Journal of Catalysis 284 (2011) 194–206

Contents lists available at SciVerse ScienceDirect

Journal of Catalysis

journal homepage: www.elsevier.com/locate/jcat

Stability and reactivity of active sites for direct benzene oxidation to phenol in Fe/ZSM-5: A comprehensive periodic DFT study

Guanna Li [a,c], Evgeny A. Pidko [b], Rutger A. van Santen [b], Zhaochi Feng [a], Can Li [a,*], Emiel J.M. Hensen [b,*]

[a] State Key Laboratory of Catalysis, Dalian Institute of Chemical Physics, Chinese Academy of Sciences, 457 Zhongshan Road, Dalian, China
[b] Inorganic Materials Chemistry Group, Schuit Institute of Catalysis, Eindhoven University of Technology, P.O. Box 513, 5600 MB Eindhoven, The Netherlands
[c] Graduate University of Chinese Academy of Sciences, Beijing 100049, China

ARTICLE INFO

Article history:
Available online 1 September 2011

Keywords:
Direct benzene oxidation
Fe/ZSM-5
Reaction mechanism
DFT calculations
Binuclear sites
N_2O dissociation
Phenolate

ABSTRACT

The stability of isolated extraframework Fe^{2+} ions in ZSM-5 zeolite and their reactivity in the benzene to phenol oxidation were studied by periodic DFT calculations. Mononuclear iron(II) cations can only be stabilized at very specific exchange sites of ZSM-5 zeolite. Accordingly, iron will be predominantly present as oxygenated/hydroxylated mono- and binuclear iron complexes in Fe/ZSM-5. The reactivity of isolated Fe^{2+} does not depend on the local coordination environment around iron, whereas the steric constraints imposed by the zeolite lattice are important for the overall catalytic reactivity. $[FeO]^+$, $[HOFe(\mu\text{-}O)FeOH]^{2+}$, $[Fe(\mu\text{-}O)_2Fe]^{2+}$, $[Fe(\mu\text{-}O)Fe]^{2+}$ extraframework complexes are also potential sites for benzene activation. The reaction is however not catalytic in these cases because the vacant active site cannot be regenerated. The presence of basic extraframework O ligands in these complexes favors phenol dissociation resulting in the formation of stable grafted phenolate species, and ultimately, to the deactivation of the oxygenated iron complexes.

1. Introduction

Zeolites are crystalline microporous aluminosilicates extensively used in the petrochemical industry. By exchanging the charge-compensating protons for transition metal cations, the chemical and catalytic properties of zeolites can be tuned so as to obtain catalysts for a wider range of reactions than only acid catalyzed ones. For instance, the introduction of Fe renders the high-silica zeolite ZSM-5 active in the catalytic decomposition of nitrous oxide (N_2O), which is a notorious greenhouse gas mainly formed as a by-product in nitric and adipic acid synthesis. Catalytic N_2O decomposition by Fe/ZSM-5 involves the formation of extraframework oxygen atoms on Fe cations followed by recombinative O_2 desorption [1–10]. Another interesting application is in the field of hydrocarbon oxidation. The Fe/ZSM-5 catalyst can oxidize methane to methanol and benzene to phenol, but only the latter reaction can be carried out in a catalytic manner so far [11–16]. There are quite some data in support of isolated Fe^{2+} ions as the active site for benzene oxidation, whereas dispersed oligonuclear and most likely binuclear Fe complexes form the active sites for catalytic N_2O decomposition [17–38]. It has also been proposed that extraframework Al and Ga species may play a role in the active sites for benzene oxidation [12,38–41]. The role of isolated Fe^{3+} and binuclear complexes in benzene oxidation is unclear. Due to the relatively heterogeneous nature of extraframework Fe species, the low concentrations of Fe^{2+} and, accordingly, the difficulty in determining the nuclearity of the Fe species in Fe/ZSM-5, a clear assignment of the active site for benzene oxidation remains moot [42–44,33].

In such case, computational modeling can assist in predicting the stability and reactivity of various Fe sites at different locations of the zeolite lattice. So far, most studies have employed cluster models. Bell et al. reported on the reaction mechanism of N_2O decomposition on different (de)hydrated mononuclear Fe sites in Fe/ZSM-5 [45–48]. Different binuclear Fe complexes have also been proposed before by several groups for N_2O decomposition. Binuclear Fe sites may form upon the self-organization of oxygenated or hydroxylated mononuclear Fe ions. The reactivity of binuclear $[HO\text{-}Fe(\mu O)Fe\text{-}OH]^{2+}$ and $[Fe(\mu O)Fe]^{2+}$ complexes for catalytic N_2O decomposition has been discussed in the literature [49–51]. An alternative diamond core $[Fe_2O_2H]^+$ complex was proposed by Kiwi-Minsker and co-workers [52–56]. A peroxide-bridged $[Fe(\mu OO)(\mu O)Fe]^{2+}$ binuclear site generated during the catalytic N_2O decomposition was also proposed [29]. Recently, Sklenak et al. investigated the reactivity for N_2O dissociation over two Fe^{2+} cations placed in two adjacent six-membered rings of Fe/ferrierite, Fe/ZSM-5, and Fe/Beta [57]. These authors concluded that the proximity of two Fe^{2+} ions at a distance of 7.4 Å in

* Corresponding authors. Fax: +86 411 84694447 (C. Li), +31 40 2455054 (E.J.M. Hensen).
E-mail addresses: canli@dicp.ac.cn (C. Li), e.j.m.hensen@tue.nl (E.J.M. Hensen).

0021-9517/$ - see front matter © 2011 Elsevier Inc. All rights reserved.
doi:10.1016/j.jcat.2011.07.008

ferrierite is essential to explain its superior catalytic activity. In the case of beta and ZSM-5 zeolites, the probability of the formation of such a specific configuration was predicted to be very low.

The first computational study on the reaction mechanism for benzene to phenol oxidation using a cluster model representing Fe/ZSM-5 was carried out by Yoshizawa et al. [58]. An isolated $[FeO]^+$ ion was used as the active site. As a model of Fe^{2+} in ZSM-5, the group of van Santen considered the ferrous ion at the α position of ferrierite to compute the potential energy diagram of the selective benzene oxidation [59]. Isolated Fe^+, Fe^{2+}, and $[FeO]^+$ ions were considered as the active sites for N_2O dissociation and benzene oxidation by Fellah et al. [60–62].

Despite substantial experimental and theoretical effort aimed at identifying the active site in Fe/ZSM-5 catalysts, the role of the different intrazeolitic iron sites in catalytic benzene to phenol oxidation as well as the actual mechanism of the catalytic reaction is still under debate. Herein, we present a comprehensive theoretical investigation of the preferred location of extraframework Fe^{2+} (ferrous ion) in ZSM-5 zeolite (Fig. 1a) and their reactivity in the catalytic oxidation of benzene to phenol. We varied the Al distribution close to the potential locations (Fig. 1b) of Fe^{2+} and also considered the situation of indirect charge compensation [63,64]. To have a basis of comparison, we included FeO^+ (ferric ion) and a number of oxo/hydroxyl-bridged binuclear complexes in our study. The reaction mechanism for benzene oxidation to phenol considered over extraframework iron species (Fe_{EF}) is schematically shown in Fig. 1c. It involves (i) the adsorption and dissociation of N_2O, (ii) the adsorption and oxidation of benzene and (iii) the desorption of phenol. Following the proposal by Fellah et al. [62], we also considered the possibility of formation of grafted phenolate complexes. The majority of works on this subject have employed clusters that represent part of the zeolite framework. Two recent studies of Sklenak et al. [57] and Benco et al. [65] have employed periodic boundary conditions for the study of N_2O decomposition by Fe^{2+} in ferrierite zeolite. Such studies are lacking for Fe/ZSM-5 with a more complex unit cell composition. Currently, calculations involving the complete unit cell of MFI zeolite are becoming accessible [66–69]. This presents an interesting possibility to determine the preferred location of the suspected active sites and to investigate the influence of the zeolitic micropores on their reactivity and ultimately to create a molecular picture of the role of different iron species in Fe/ZSM-5 catalyst in transformations of benzene to phenol.

2. Computational details

Quantum chemical calculations were performed using density functional theory (DFT) as implemented in the Vienna Ab Initio Simulation Package (VASP) [70–73]. The projected augmented waves (PAW) method was used to describe electron–ion interactions [74,75]. For the exchange and correlation energies, the PBE

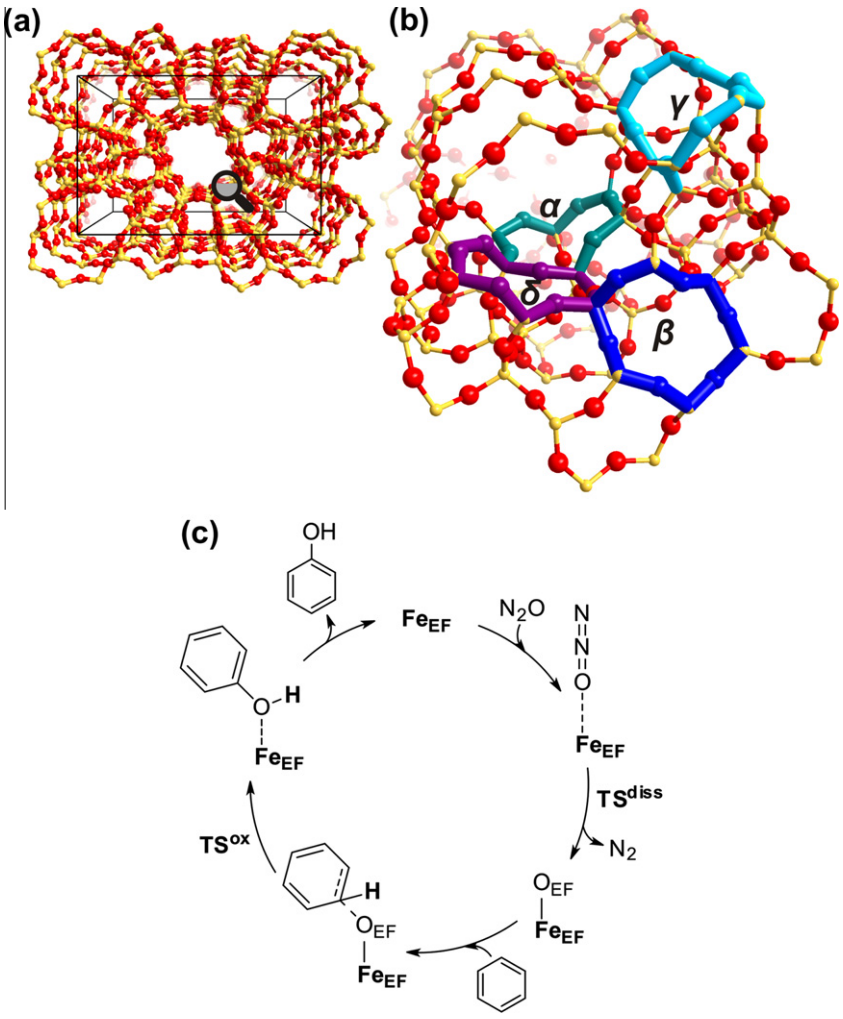

Fig. 1. The structure of ZSM-5 zeolite (a) and the relative location of selected cation sites in it (b). (c) depicts a catalytic cycle for benzene to phenol oxidation with N_2O over extraframework iron (Fe_{EF}) sites.

form of the generalized gradient approximation was employed [76]. Brillouin zone-sampling was restricted to the Γ point [77]. The energy cutoff was set to 400 eV. Full geometry optimization was performed with fixed optimized cell parameters using a conjugated gradient algorithm. Convergence was assumed, when the energy change was smaller than 10^{-4} eV between two ionic steps. A modest Gaussian smearing was applied to band occupations around the Fermi level, and the total energies were extrapolated to $\sigma \rightarrow 0$. In the first step, the cell parameters were optimized for the all-silica MFI orthorhombic structure ($Si_{96}O_{192}$) [78]. The parameters after optimization of volume and shape were as follows: a = 20.119, b = 19.767 and c = 13.161 Å, which corresponds very well to the experimental XRD data of a = 20.090 Å, b = 19.738 Å, and c = 13.142 Å [79]. By replacing two of the 96 unit cell silicon atoms by two Al atoms, a ZSM-5 lattice with a Si/Al ratio of 47 was obtained. In the case of FeO^+ species, a single framework Al atom was introduced in the unit cell (Si/Al = 95). The negative charge of the resulting anionic sites was compensated by extra-framework iron cations. Mononuclear Fe^{2+} and $[FeO]^+$ as well as binuclear $[Fe(\mu\text{-}O)Fe]^{2+}$, $[Fe(\mu\text{-}O)_2Fe]^{2+}$ and $[HOFe(\mu\text{-}O)FeOH]^{2+}$ extraframework complexes were considered as charge-compensating species. All calculations were performed with a fixed spin multiplicity corresponding to the most stable configuration of the initial iron complex (see Supporting Information). The lowest energy electronic configuration for Fe^{2+} is S = 4/2. For the dimeric $[Fe(\mu\text{-}O)Fe]^{2+}$, $[Fe(\mu\text{-}O)_2Fe]^{2+}$ and $[HOFe(\mu\text{-}O)FeOH]^{2+}$ complexes, the ferromagnetic S = 8/2 state was found to be the most stable. It should be noted that in the case of binuclear Fe(III) clusters, the high-spin states S = 6/2, S = 8/2 and S = 10/2 do not differ much in energy. The spin state has previously been shown to only have a minor influence on the reaction mechanism [50]. To confirm this, the reactivity of the mononuclear $Fe(III)O^+$ species was compared for the most stable S = 5/2 and the less stable S = 3/2 states.

The nudged elastic band method (NEB) with improved tangent estimate was used to determine the minimum energy path and to locate the transition-state structures [80]. The maximum energy geometries obtained with the NEB method were further optimized using a quasi-Newton algorithm. In this step, only the extraframework atoms were relaxed. Frequency analysis of the stationary points was performed by means of the finite difference method as implemented in VASP. Small displacements (0.02 Å) were used to estimate the numerical Hessian matrix. The transition states were confirmed by the presence of a single imaginary frequency corresponding to the reaction path.

The energetics as computed with DFT was further corrected for dispersion interactions by adding the contributions from van der Waals bonds between the confined hydrocarbon species and the zeolitic matrix. These interactions were estimated by computing an additional interatomic Lennard–Jones potential for the DFT-optimized structures as defined in the consistent valence force field (CVFF) [81,82] with the approach as proposed by Demuth et al. [83] and Vos et al. [84] using the GULP program [85]. The consistent valence force field (CVFF) is known to accurately describe trends involving dispersive interactions of hydrocarbons in zeolite pores [86,87]. This methodology has recently been successfully employed for the description of the zeolite-catalyzed hydrocarbon conversion [68,69]. For all structures including the local minima and transition states, two subsystems were defined within the DFT-optimized periodic system, representing the hydrocarbon moiety and the zeolite. The vdW interaction between these subunits represents the vdW stabilization of the confined hydrocarbon species. Previous studies have shown that the addition of the empirical corrections to the results obtained at the PBE level results in both thermodynamic and kinetic parameters that are very close to those obtained at the higher ab initio level [88].

3. Results

3.1. Mononuclear iron species as the active site in benzene oxidation

3.1.1. Location of Fe^{2+} and $[FeO]^{2+}$ in ZSM-5

With the goal to determine the most stable location of extra-framework mononuclear Fe^{2+} and $[FeO]^{2+}$ in the zeolite micropores, we considered a large number of models with different locations for the Al^{3+} substitutions in the zeolite framework. The α- and β-sites represent a six-membered ring (6MR) in the straight channel and a deformed 6MR at the intersection of straight and sinusoidal channels, respectively [89]. In our investigations, we additionally considered a 6MR site that is located at the intersection of the straight and sinusoidal channels (δ-site, Fig. 1b). The T atom arrangement of this δ-site differs from that of the α-site in that the bridging connection between opposite sides of the 6MR contains two T atoms in the former and one in the latter. Further sites considered are in the double five-membered rings (D5MRs), which are part of the zeolite walls. These sites have been investigated before as cation exchange sites for stabilization of Zn [90], Ga [91,92], and Fe [50,55,56,61] as mononuclear exchangeable cations and also as oxygenated complexes. Finally, we included an adsorption site close to the eight-membered ring (8MR) moiety at the wall of the sinusoidal channel composed of two interconnected 5MR (γ site). For each of these sites, we considered different configurations of the framework substitutions. Selected geometrical parameters and relative stabilities of Fe^{2+} at different local configurations of ZSM-5 are summarized in Table 1. The corresponding relevant portions of the optimized zeolite models containing Fe^{2+} are displayed in Figs. 2 and 3.

For each of the three 6MR models, three different configurations of the framework substitutions are compared. The most stable configuration is the one involving Fe^{2+} located in a δ-site (δ-1) with the framework Al atoms at two T11 positions, resulting in a symmetric distribution of the charge-compensating anionic sites over the zeolite 6MR (Fig. 3, top panel). As a result, the ferrous ion is bonded through four equivalent bonds with the zeolite lattice. The four Fe–O_F (O_F represents framework oxygen) have similar bond lengths close to 2.034 Å. The perturbations of the zeolite lattice in this case are smaller when compared to the less stable sites.

When Fe^{2+} is located at the α-site with a similar distribution of the Al atoms, an additional bond between the cation and one of the oxygen anions below the 6MR is formed (Fig. 3, middle panel). Despite the higher coordination number of the resulting distorted square-pyramidal configuration, this configuration is less favorable by 64 kJ/mol as compared to Fe^{2+} at the δ-1 site. The difference is due to the more substantial deformations of the zeolite framework resulting from the coordination of Fe^{2+} to the α-1 site and the lower flexibility of this portion of the zeolite lattice. As a result, the average Fe–O_F distance is approximately 0.12 Å longer compared to Fe^{2+} at the δ-1 site (Table 1).

The δ-2 and α-2 configurations involve Al substitutions at the opposite corners of the 6MRs (Figs. 2 and 3). These structures exhibit comparable stabilities in the presence of Fe^{2+} to that of the α-1 configuration and likewise result in substantial local deformations of the zeolite lattice upon introduction of the cation (Table 1). Similar to δ-1, Fe^{2+} forms four Fe–O_F bonds at the δ-2 site, but they are not uniform. One of the Fe–O_F bonds is much longer (2.767 Å) than the others. The average Fe–O_F bond length is 0.15 Å longer compared to that in the configuration δ-1. In addition, strong local deformation of the zeolite framework is observed for both δ-2 and α-2 configurations.

The least stable of the α- and δ-site configurations involves the framework Al atoms at next-nearest positions within the 6MR (Figs. 2 and 3). This is mainly caused by the coordination of Fe^{2+}

Table 1
Calculated Fe–O bond lengths and relative stabilities of different configurations of Fe^{2+}/ZSM-5.[a].

Configuration		Fe–O bond lengths	Fe–O (avg)	Relative stability
Type of site	T sites of Al/Si			
δ-site				
δ-1	T11,T11	2.033, 2.034, 2.034, 2.036	2.034	0
δ-2	T12,T7_diag[c]	1.926, 1.954, 2.081, 2.767	2.182	68
δ-3	T12,T7_ASA[d]	1.994, 2.019, 2.118, 2.146	2.069	119
β-site				
β-1	T4,T10	2.003, 2.019, 2.029, 2.050	2.025	36
β-2	T1,T7	2.010, 2.078, 2.188, 2.158, 2.423	2.171	93
β-3	T5,T11	1.917, 2.006, 2.170, 2.216	2077	106
α-site				
α-1	T1,T7	2.007, 2.129, 2.132, 2.376, 2.123[b]	2.153	64
α-2	T2,T11	2.040, 2.060, 2.117, 2.269, 2.185[b]	2.134	66
α-3	T2,T5	1.977, 2.013, 2.165, 2.252[b]	2.102	129
D5MR				
D-1	T3,T9	1.952, 1.977, 2.090, 2.110	2.032	92
D-2	T2,T9	1.970, 2.028, 2.035, 2.120	2.038	98
D-3	T12,T5	2.016, 2.161, 2.163, 2.331	2.168	115
D-4	T12,T9	1.932, 2.010, 2.085, 2.145	2.043	200
γ-site				
γ-1	T7,T12_Fe@8MR	2.001, 2.061, 2.073, 2.118	2.063	57
γ-2	T7,T12_Fe@6MR	1.969, 2.095, 2.143, 2.178	2.096	178
α-5MR				
	T7,T12_Fe@6MR	1.986, 2.121, 2.254, 2.120[b]	2.265	187
	T7,T12_Fe@5MR	2.014, 2.024, 2.063, 2.158	2.065	225
	T1,T12_Fe@6MR	2.064, 2.098, 2.108, 2.498, 2.130[b]	2.180	176
	T1,T12_Fe@5MR	2.004, 2.055, 2.062, 2.112	2.058	221
	T2,T12_Fe@6MR	2.025, 2.133, 2.219, 2.257, 2.140[b]	2.155	181
	T2,T12_Fe@5MR	2.032, 2.049, 2.055, 2.136	2.068	255

[a] Interatomic distances (<2.5 Å) are given in angstroms and relative stabilities are in kJ/mol.
[b] Fe–O bond lengths between Fe^{2+} and bridging oxygen of α site.
[c] Configuration contains a chain sequence –Al–Si–Si–Al–.
[d] Configuration contains a chain sequence –Al–Si–Al–.

to two oxygen anions of $[AlO_2]^-$ sites instead of four in the configurations discussed above. The coordination of Fe^{2+} is completed by less basic $[SiO_2]$ sites. For the δ-3 configuration, this results in a lower stability by 119 kJ/mol as compared to the δ-1 configuration. In this case, the deformations of the zeolite framework are minor, and the average Fe–O bond length is 2.069 Å. In the α-3 configuration, the strongly asymmetric location of the framework Al ions results in a decrease of the Fe–O_F coordination to four and substantial structural deformations. The energies of the α-3 and δ-3 configurations are comparable. Fe^{2+} interacts more strongly with the basic $[AlO_2]^-$ units of the α-3 configuration, which partially compensates for the substantial energy losses due to lattice deformation.

The trends in stability of Fe^{2+} upon coordination to the β-site are similar. The most stable site is the one providing a relatively symmetric coordination environment (β-1 configuration) with the Al substitutions at T4 and T10 positions. This site is the second most stable configuration among the models considered here. It is only 36 kJ/mol less stable than the δ-1 configuration. The average Fe–O_F bond length is 2.025 Å. The β-2 and β-3 configurations result in substantial deformation of the zeolite lattice and are therefore less stable by 93 and 106 kJ/mol, respectively. The β-2 configuration with Al placed at T1 and T7 positions results in five Fe–O_F bonds that allow a slightly better stabilization of Fe^{2+} as compared to the β-3 configuration having four Fe–O_F bonds.

We have also considered the stabilization of Fe^{2+} within double five-membered ring structures of ZSM-5 (D5MR, D1–D4 configurations, Fig. 2, Table 1). Four different framework Al distributions were considered. When the positive charge of the Fe^{2+} cation is compensated through a direct coordination bond with two anionic $[AlO_2]^-$ framework sites, the relative stabilities of the resulting D-1, D-2 and D-3 configurations are 92, 98 and 115 kJ/mol, respectively (Fig. 2). The lower stabilities of these configurations as compared to that of the 6MR sites are due to the higher rigidity of this part of the zeolite framework. The least stable configuration (200 kJ/mol) is found when one of the two charge-compensating $[AlO_2]^-$ lattice anions does not directly interact with the exchangeable cation (configuration D-4).

A further configuration is constructed by placing Al atoms at T7 and T12 positions within an 8MR unit. In this case, we compared two possible locations of Fe^{2+}, *i.e.*, within the 8MR (γ-1) or in the neighboring 6MR, which is a δ-site (γ-2) (Fig. 2). The former structure is more stable by ~120 kJ/mol than the γ-2 configuration. This resembles the energy differences found for different Al distributions in D5MRs. The stability of the extraframework Fe^{2+} cation critically depends on the possibility of direct charge compensation. The relative energy of the configuration γ-1 as compared to that of δ-1 is 57 kJ/mol. This is comparable to the value computed for the α-1 configuration. Thus, the 8MR site can also be considered a favorable candidate for the location of Fe^{2+}.

For completeness, we considered additional Fe/ZSM-5 configurations involving the stabilization of Fe^{2+} at 5MR or 6MR with the two charge-compensating $[AlO_2]^-$ sites occupying lattice positions in adjacent zeolite rings (Fig. 2, bottom panels). In these cases, Fe^{2+} was placed in the vicinity of one of the $[AlO_2]^-$ units, whereas the other negative framework site was located at a larger distance where it did not directly interact with the extraframework cation. The calculations predict very low stability for such configurations (Table 1, α-5MRs).

The hydroxylation of benzene to phenol involves the prior dissociation of nitrous oxide to produce an extraframework electrophilic oxygen atom (O_{EF}). To evaluate the role of the local zeolite

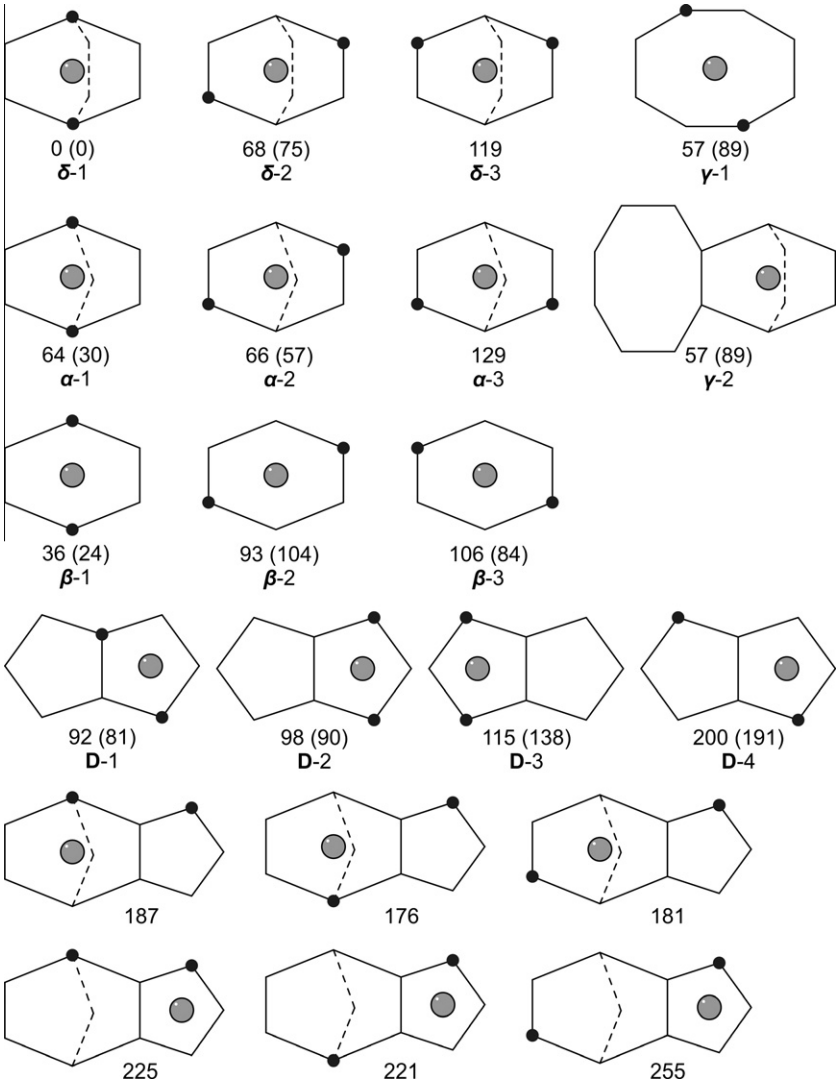

Fig. 2. Schematic representation of different cation sites of ZSM-5 zeolite with two lattice Al atoms (black spheres) and a single Fe ion (gray sphere). Relative stability (in kJ/mol) of Fe^{2+} and FeO^{2+} (values in brackets) species at a particular local configuration is given with respect to the δ-1 configuration.

environment, we computed the stability of $[FeO]^{2+}$ located at a number of favorable configurations for Fe^{2+} (δ-1, δ-2, α-1, α-2, β-1, β-2, β-3, γ-1). Despite their earlier established lower stability to accommodate Fe^{2+}, we also consider the D5MRs sites, because these sites are often employed in cluster simulations. The relative energies of the different locations of $[FeO]^{2+}$ and the corresponding optimized Fe–O bond lengths are collected in Table 2. Similar to Fe^{2+}, the δ-1 configuration is the most favorable location for $[FeO]^{2+}$. Configurations β-1 and α-1 result in somewhat lower stability by 24 and 30 kJ/mol, respectively, while $[FeO]^{2+}$ at D5MRs, units represent the least favorable configurations.

In summary, both Fe^{2+} and $[FeO]^{2+}$ are preferentially located at the α- and δ-sites in the main channel and at the β-site at the intersection of the straight and sinusoidal channels. The most stable location of Fe^{2+} and $[FeO]^{2+}$ in ZSM-5 zeolite is the symmetric configuration formed by Fe^{2+} in the 6MR with two $[AlO_2]^-$ units at the T11 lattice positions at the intersection of the straight and sinusoidal channel. Configurations of somewhat lower stability involve the 6MR at the α- and β-sites. Fe^{2+} at the 8MR of the sinusoidal channel is moderately stable. Locations of Fe^{2+} within 5MR sites or involving indirect charge compensation are generally much less stable. The location of Fe^{2+} strongly depends on the possibility to form direct bonds between Fe^{2+} and framework oxygen atoms of the aluminum-occupied oxygen tetrahedra. The flexibility of the local framework environment is a further factor contributing to the stability of a particular configuration. The preferred location of Fe^{2+} in δ-, α- and β-6MRs sites is in agreement with the experimental findings for Co^{2+} and Cu^+ ions in ZSM-5 [89,93]. The preference for the presence of isolated Fe^{2+} at 6MR sites is in line with the previous theoretical results on the stabilities of Fe^{2+} in ferrierite, Zn^{2+} in mordenite and Cu^+ in ZSM-5 [94–96].

3.1.2. Reaction mechanism of benzene oxidation on Fe^{2+} and $[FeO]^+$ in ZSM-5

We computed the reaction energy diagrams based on the following reaction mechanism (Fig. 1c) for the oxidation of benzene to phenol with N_2O. First, N_2O molecule adsorbs physically on Fe^{2+} followed by its dissociation, resulting in $[FeO]^{2+}$ and gaseous N_2. Subsequently, benzene interacts with the extraframework oxygen atom, resulting in the formation of a pre-activated adsorbed complex, which is the precursor for the subsequent oxidation step. After oxidation, the catalytic cycle closes by desorption of phenol from the coordination complex with Fe^{2+}. We considered benzene oxidation starting from Fe^{2+} located at δ-1, α-1 and β-1 site. As the oxidation state of the active Fe centers in Fe/ZSM-5 catalysts has not been unequivocally established, we also included

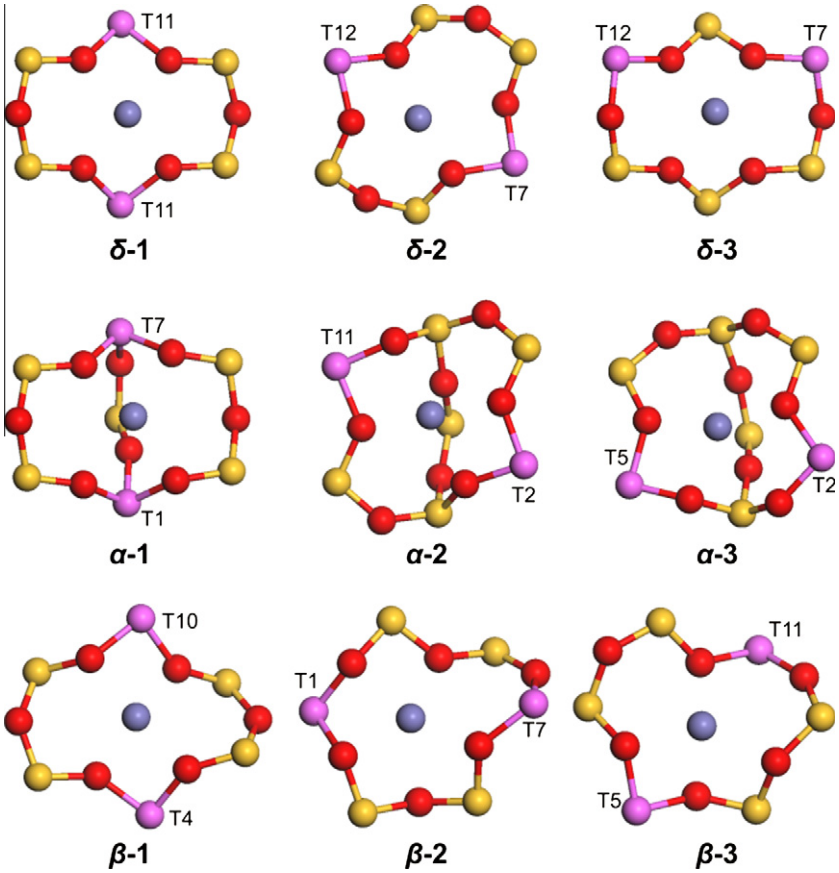

Fig. 3. Optimized structures of Fe^{2+} stabilized at 6MR cation sites in ZSM-5.

Table 2
Calculated Fe–O bond lengths and relative energies of $[FeO]^{2+}$/ZSM-5.[a].

Configuration		Fe–O bond lengths	Fe–O_F[b]	Fe–O_{EF}[c]	Relative stability
Type of site	Locations of Al				
δ-site					
δ-1	T11,T11	2.032, 2.034, 2.042, 2.044	2.038	1.618	0
δ-2	T12,T7_diag[d]	1.914, 1.933, 2.096	1.981	1.619	75
α-site					
α-1	T1,T7	2.018, 2.108, 2.138, 2.253, 2.137[e]	2.131	1.629	30
α-2	T2,T11	2.076, 2.088, 2.103, 2.169, 2.236[e]	2.134	1.623	57
β-site					
β-1	T4,T10	2.004, 2.032, 2.048, 2.057	2.035	1.629	24
β-2	T1,T7	1.990, 2.120, 2.147, 2.265, 2462	2.197	1.619	104
β-3	T5,T11	1.996, 2.020, 2.052, 2.105	2.043	1.630	84
γ-site					
γ-1	T12,T7_Fe@8MR	1.954, 1.966, 2.095, 2.162	2.044	1.633	89
D5MRs					
D-1	T3,T9	1.957, 1.978, 2.089, 2.113	2.034	1.619	81
D-2	T2,T9	1.972, 2.034, 2.036, 2.131	2.043	1.619	90
D-3	T12,T5	1.912, 2.023, 2.053, 2.201	2.047	1.632	138
D-4	T12,T9	1.907, 2.052, 2.074, 2.139	2.043	1.620	191

[a] Interatomic distances (<2.5 Å) are given in angstroms, and relative stabilities are in kJ/mol.
[b] Average distances between the Fe center and framework O atoms.
[c] Fe–O bond length in the extraframework FeO^{2+} species.
[d] Interatomic distance between Fe^{2+} and the framework bridging oxygen of the α site.
[e] Lattice configuration contains a sequence –Al–Si–Si–Al–.

mononuclear Fe^{3+} species in our calculations. Similar to previous experimental [45,97] and theoretical [62,98,99] studies, we considered $[FeO]^+$ as the active complex and carried out comparable calculations of reaction energy diagrams for $[FeO]^+$ stabilized at the δ-1 site containing one Al substitution at the T11 lattice position. The consideration of a single cation site in this case is justified by the weak influence of the local zeolite environment on the geometrical properties and reactivity of the monovalent $[FeO]^+$ species

[62,98–100]. The local optimized geometries of all reaction intermediates and transition states are shown in the Supporting information.

The reaction energy diagram for the oxidation of benzene to phenol by nitrous oxide catalyzed by Fe^{2+} at the δ-1 site is shown in Fig. 4. Adsorption of N_2O is slightly exothermic with $\Delta E_{ads} = -9$ kJ/mol. Subsequent dissociation of the N–O bond and the formation of $[FeO]^{2+}$ and N_2 is thermodynamically favored ($\Delta E = -57$ kJ/mol). The main entropic contribution to the reaction free energy in this case is due to the rather small entropy difference between the gas-phase N_2O and N_2 (estimated $T\Delta S = 15$ kJ/mol at $T = 623$ K). Thus, the free reaction energies should be quite close to the reaction enthalpies. Accordingly, this implies that the oxidation reaction of Fe^{2+} by N_2O will go to completion under the typical conditions employed for titration of Fe^{2+} sites in Fe/ZSM-5 [23,38].

N_2O dissociates with an activation barrier of only 59 kJ/mol. This value is close to the experimental value of 70 kJ/mol [101] and is somewhat lower than the value of 83 kJ/mol computed using a cluster model representing Fe^{2+} in a D5MRs unit [61]. The N_2 molecule interacts very weakly with $[FeO]^{2+}$. Physical adsorption of N_2O on Fe^{2+} leads to elongation of Fe–O_F bonds to 2.046–2.119 Å. The average Fe–O_F distance equals 2.075 Å. Because of the increase of the formal charge and, consequently, of the Lewis acidity of the iron cation, dissociation of N_2O results in shortening of the Fe–O_F distances to 2.032–2.044 Å, and the average bond length is 2.038 Å. The Fe–O_{EF} bond length is 1.62 Å. In this configuration, $[FeO]^{2+}$ forms an almost perfect square–pyramidal coordination environment of the iron cation. The perturbations of the local framework geometry following N_2O dissociation are very small. Further oxidation of $[FeO]^{2+}$ by N_2O resulting in $[FeO_2]^{2+}$ cations is very unlikely with a calculated energy difference of $\Delta E = +109$ kJ/mol. The high endothermicity is due to the highly unfavorable oxidation of formally Fe(IV) to Fe(VI) and the severe distortions resulting from the additional O ligand in the coordination sphere of iron.

The next step involves the adsorption of benzene on the extra-framework oxygen atom of $[FeO]^{2+}$. Structural changes in the benzene ring point to a partial loss of the aromaticity and the formation of a σ-complex. One of the C–H bonds is elongated and protrudes from the initial plane of the benzene ring. The extra-framework oxygen atom forms a bond with this carbon atom at a distance of 1.425 Å. The reaction energy (ΔE^{PBE}) for the formation

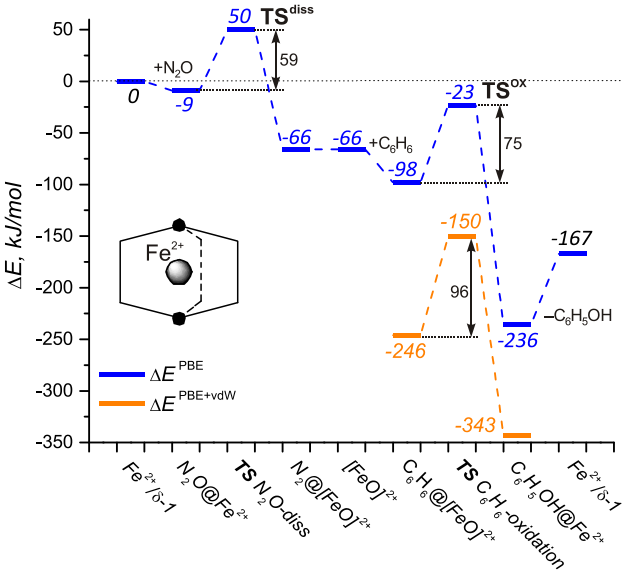

Fig. 4. Reaction energy diagram for benzene oxidation to phenol by N_2O on mononuclear Fe^{2+} at the δ-1 site of ZSM-5.

of this activated complex is −32 kJ/mol. The activation barrier for phenol formation of 75 kJ/mol is substantially higher than the value of 41 kJ/mol predicted for Fe^{2+} stabilized in a D5MRs cluster [61]. Subsequent desorption of phenol and regeneration of the active Fe^{2+}/δ-1 site is endothermic. The reaction energy (ΔE^{PBE}) equals 69 kJ/mol for this step. This is almost twice lower as compared to the value reported by Fellah et al. [61]. The large deviations between our results and those obtained previous by Fellah et al. using a cluster modeling approach are due to the more realistic representation of the intrazeolite environment by a periodic Fe/ZSM-5 model and the resulting substantial repulsive interactions between the confined hydrocarbon intermediates and the zeolitic walls.

Addition of the vdW contributions to the calculated energies ($\Delta E^{PBE+vdW}$) has a pronounced effect on the overall energy profiles, although the qualitative picture for the individual reaction steps remains unchanged (Fig. 4). The influence of dispersive interactions is negligible for the transformations involving N_2O, and these have therefore not been included. As the interaction between hydrocarbons and the zeolite oxygen anions is predominantly dispersive, substantial corrections were obtained for the states involving benzene and phenol in the zeolite micropores. The inclusion of these dispersive interactions makes the complete evacuation of phenol from the zeolite matrix much more endothermic ($\Delta E^{PBE+vdW} = 176$ kJ/mol) compared to the intrinsic barrier for benzene oxidation (96 kJ/mol). Obviously, the correction for the latter activation barrier is minor as compared to the desorption step, because of the similar magnitude of the van der Waals stabilization of benzene and phenol in the zeolite channels.

Geometry optimization of $[FeO]^+$ at the δ-1 site containing a single framework Al substitution at the T11 site results in a three-coordinated complex with two Fe–O_F bonds. The complex is located above the plane of the 6MR unit of the δ-1 site. We considered the high ($S = 5/2$) and low spin ($S = 3/2$) states of Fe(III). The energy differences between these electronic configurations are 21 kJ/mol with a preference for the high-spin state. Fig. 5a and b gives the reaction energy diagrams for benzene oxidation for the high and low spin states, respectively. The low spin structure of $[OFeO]^+$ formed upon the dissociative adsorption of N_2O is more stable than the high-spin equivalent. This result implies a very low barrier for spin flip depending on the specific coordination environment and the presence of adsorbates. The energy barriers for N_2O dissociation are 94 ($S = 5/2$) and 73 ($S = 3/2$) kJ/mol, while the respective values for the benzene oxidation are 48 and 51 kJ/mol. The adsorption energy (ΔE^{PBE}) of benzene on the $[FeO]^+/\delta$-1 site is endothermic because of repulsive interactions with the zeolite framework. When the vdW interactions are taken into account, the formation of the adsorption complex becomes more favorable ($\Delta E^{PBE+vdW}$). Consequently, the barriers for benzene oxidation are around 25 kJ/mol for both spin states ($\Delta E^{PBE+vdW}$). Likewise, the desorption energies of phenol become comparable to the values reported above for the $[FeO]^{2+}$ site after inclusion of the dispersive interactions.

An important intermediate conclusion is that the activation barrier for benzene oxidation by the $[OFeO]^+$ intermediate (~25 kJ/mol) is substantially lower than the corresponding barrier by the $[FeO]^{2+}$ intermediate (96 kJ/mol). However, an alternative pathway leading to the deactivation of the reactive complex competes with phenol desorption. This competing path involves proton transfer from the adsorbed phenol to the adjacent terminal O ligand at the Fe^{3+} center, resulting in the formation of a $[HO\text{-}Fe\text{-}OPh]^+$ hydroxyphenolate complex (Scheme 1). This reaction is strongly exothermic and proceeds with a low activation barrier of 36 and 19 kJ/mol for the high and low spin states, respectively. The formation of such hydroxyphenolate species stabilizes the system by 131 ($S = 5/2$) and 96 ($S = 3/2$) kJ/mol as compared to the adsorption complex of phenol

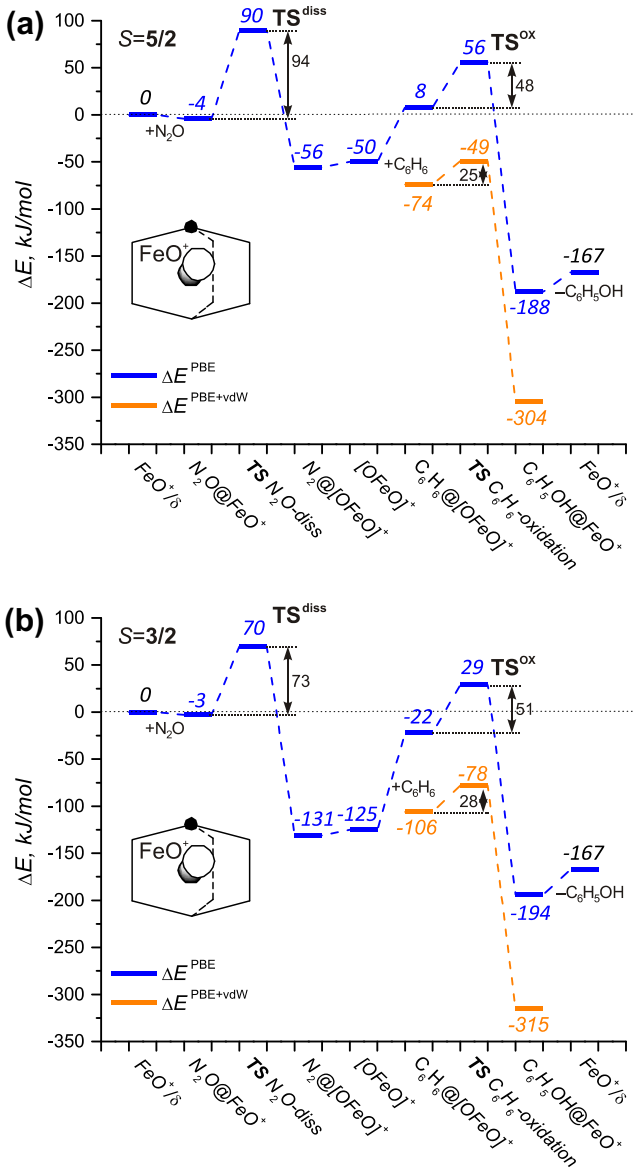

Fig. 5. Reaction energy diagrams for benzene oxidation to phenol by N_2O over mononuclear FeO^+ in (a) high-spin state ($S = 5/2$) and (b) low-spin state ($S = 3/2$).

with $[FeO]^+$. As a result, in the case of the high-spin reaction path, the energy required for the complete regeneration of $[FeO]^+$/ZSM-5 from the grafted phenolate complex exceeds 250 kJ/mol. These results imply that the benzene oxidation over mononuclear $[FeO]^+$ is a stoichiometric reaction producing a highly stable grafted intermediate that blocks the catalytic process.

Note that there also exists a possibility for the dissociation of phenol over the mononuclear Fe^{2+} sites. In this case, the basic O atoms from the $[AlO_2]^-$ lattice units of the zeolite framework play the role of proton accepting sites. Such a dissociation results in the formation of a formally monovalent $[Fe^{II}\text{-}OC_6H_5]^+$ species and a Brønsted acid site. We calculated the thermodynamics of this reaction over the Fe^{2+}/δ-1 site. To minimize repulsion between two cationic species in one zeolitic ring, the acidic proton was located at a 6MR site neighboring the δ-1 site accommodating the $[Fe^{II}\text{-}OC_6H_5]^+$ phenolate complex (see Supporting information). The reaction energy for the dissociation of phenol over the Fe^{2+}/δ-1 site is 90 kJ/mol. This implies that the activation barrier will be higher than this value of 90 kJ/mol, and, accordingly, this pathway can be excluded, because it significantly exceeds the interaction energy between phenol and Fe^{2+} (E_{ads}^{PBE}).

Benzene oxidation with N_2O over the less stable Fe^{2+} configurations β-1 and α-1 of Fe/ZSM-5 was considered in order to probe the influence of the local zeolitic environment on the catalytic reactivity of the mononuclear Fe^{2+} sites. The corresponding reaction energy diagrams are shown in Figs. 6 and 7. In both cases, the coordination environment of the iron species is substantially distorted resulting in the enhancement of the Lewis acidity of the exchangeable cation. This is evident from the much strong molecular adsorption of the weakly basic N_2O reactant compared to the more stable δ-1 configuration. The calculated N_2O adsorption energies are equal to −39 kJ/mol and −38 kJ/mol, respectively, for configurations β-1 and α-1. Subsequent formation of the oxygenated iron sites via N_2O dissociation is exothermic (ΔE = −46 and −67 kJ/mol for β-1 and α-1, respectively) and proceeds with an activation energy of about 80 kJ/mol in both cases. The interaction between N_2 and the product $[FeO]^{2+}$ ion is very weak.

Subsequent benzene coordination to the $[FeO]^{2+}$ species at configurations β-1 and α-1 is endothermic (ΔE^{PBE} = 26 and 43 kJ/mol, respectively) according to PBE calculations. These energy losses are mainly associated with the repulsion due to the unfavorable location of the benzene molecule upon interaction of $[FeO]^{2+}$ at these sites. The specific local zeolite environment decreases the accessibility of the active site. The energy losses due to the steric repulsion are to a large extent compensated when the attractive dispersion interactions are taken into account. After vdW correction, the adsorption energies ($\Delta E^{PBE+vdW}$) equal −67 and −75 kJ/mol, respectively for α-1 and β-1 configurations. The activation energy for the H transfer from the adsorbed benzene to the extra-framework oxygen and the formation of phenol are 71 and 79 kJ/mol before and after vdW correction for the β-1 configuration, while corresponding values for the α-1 configuration are 75 and 80 kJ/mol. Phenol desorption and the regeneration of the active sites is endothermic. The vdW-corrected phenol desorption energies for Fe^{2+}/α-1 and Fe^{2+}/β-1 sites equal 140 and 121 kJ/mol, respectively.

Summarizing, activation barriers and reaction energies for benzene oxidation over mononuclear Fe^{2+} stabilized at α-1, β-1 and δ-1 sites are quite similar. This implies that the intrinsic properties of the nucleophilic oxygen species formed upon the N_2O dissociation over the exchangeable Fe^{2+} cations depend only slightly on the stability of the catalytic sites and their coordination environment. The formation of phenol on $[FeO]^+$ also proceeds with relatively low activation barrier. However, in this case, a pathway leading to deactivation by formation of a hydroxyphenolate complex is strongly favored. Direct desorption of phenol from this state is negligible.

3.2. Binuclear iron sites as the active site for benzene oxidation

3.2.1. Choice of binuclear Fe clusters

We further considered three binuclear iron complexes for benzene oxidation with N_2O, namely (i) hydroxylated $[HOFe(\mu\text{-}O)FeOH]^{2+}$, which can be readily formed by condensation of two isolated $[Fe^{III}(OH)_2]^+$ species [35,50,102,103], (ii) the diamond-shaped $[Fe(\mu\text{-}O)_2Fe]^{2+}$ core resulting from the self-organization of two $[Fe^{III}O]^+$ species [58] and (iii) the mono-oxygen-bridged $[Fe(\mu\text{-}O)Fe]^{2+}$ species formed by condensation and dehydration of two $[Fe^{II}OH]^+$ ions [104,105]. The first two complexes contain two Fe^{3+} ions, while the latter complex is composed of two Fe^{2+} cations. The binuclear Fe complexes are located at the 8MR along the sinusoidal channel of ZSM-5 (γ site, Fig. 1b). This site has previously been considered for the stabilization of binuclear cationic species in ZSM-5 zeolite [106]. The larger size and specific shape of this site allows the formation of a favorable coordination environment around both Fe centers, resulting in the efficient stabilization of the relatively large binuclear complex. To

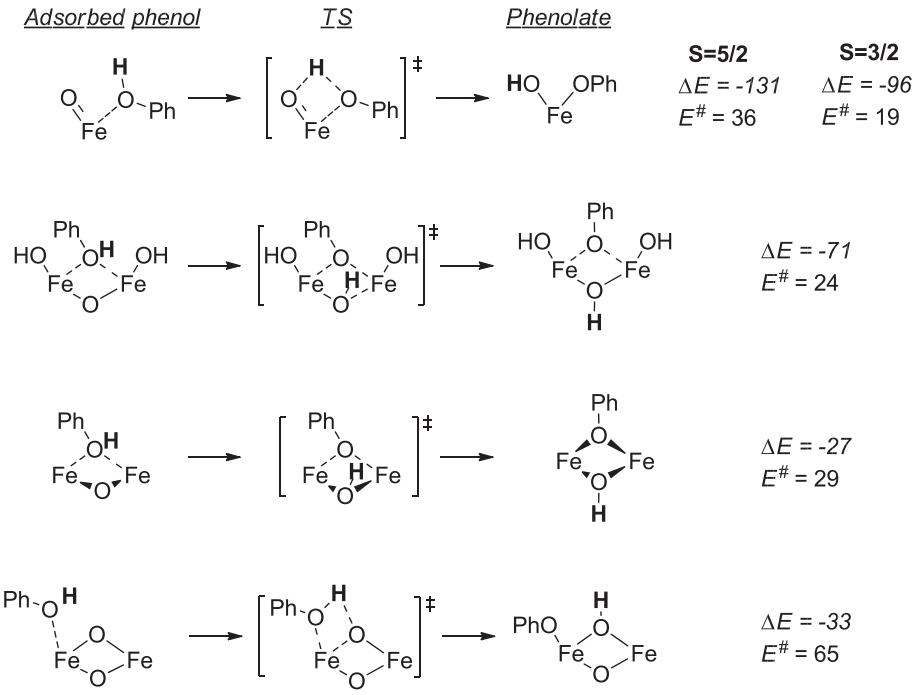

Scheme 1. Dissociation of adsorbed phenol and the formation of grafted phenolates on oxygenated iron complexes in ZSM-5 (reaction energies (ΔE) and activation barriers ($E^{\#}$) are in kJ/mol).

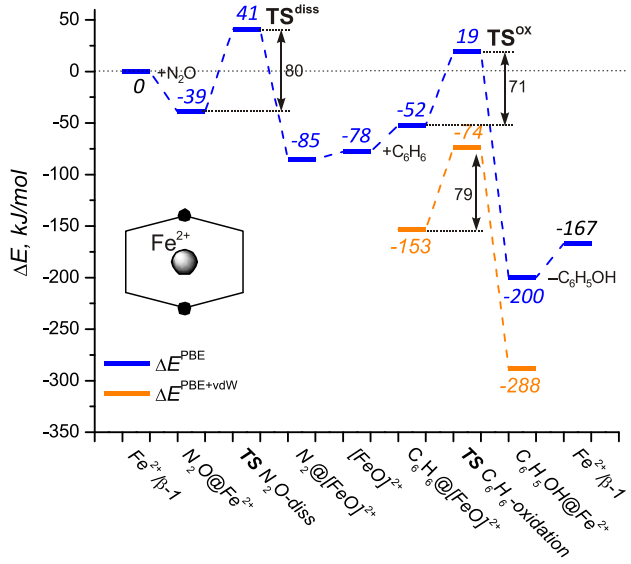

Fig. 6. Reaction energy diagram for benzene oxidation to phenol by N_2O on mononuclear Fe^{2+} at the β-1 site of ZSM-5.

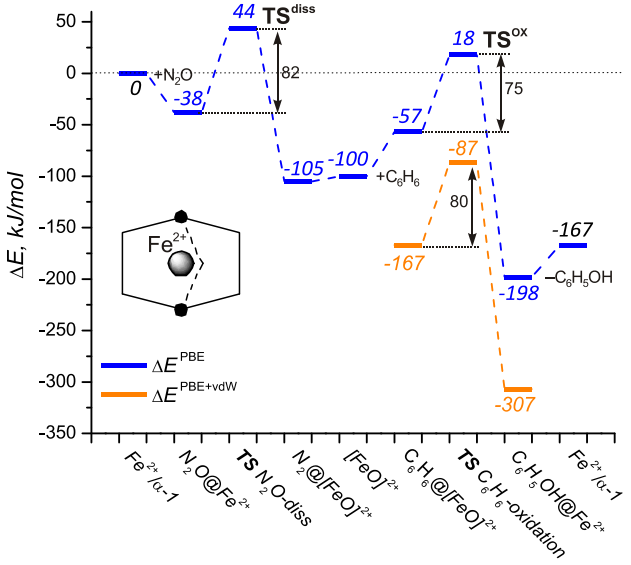

Fig. 7. Reaction energy diagram for benzene oxidation to phenol by N2O on mononuclear Fe^{2+} at the α-1 site of ZSM-5.

compensate for the 2 + charge of these extraframework cationic complexes, two framework Al substitutions were introduced at T7 and T12 framework sites.

3.2.2. Reaction mechanism of benzene oxidation on [HOFe-(μ-O)FeOH]$^{2+}$

The optimized geometry of [HOFe(μ-O)FeOH]$^{2+}$ at the 8MR of the ZSM-5 zeolite is shown in Fig. 8. Each Fe cation is coordinated by four O atoms, two of which belong to the zeolite lattice. The reaction energy diagrams for catalytic oxidation of benzene with N_2O over this complex are shown in Fig. 9. The initial N_2O dissociation over [HOFe(μ-O)FeOH]$^{2+}$ results in the [HOFe(μ-O)$_2$FeOH]$^{2+}$ complex. The activation barrier in this case is nearly twice as high as compared to the mononuclear iron sites considered above. The reaction energy is also less exothermic. The activation barrier for N_2O dissociation of 136 kJ/mol is somewhat lower than the value for a similar complex stabilized at a double 5MRs cluster model of 157 kJ/mol [50]. Subsequent benzene oxidation by the oxygenated [HOFe(μ-O)$_2$FeOH]$^{2+}$ complex is energetically more favorable as compared to the case of mononuclear Fe^{2+} sites. This reaction step proceeds with an activation barrier of only 31 kJ/mol and a reaction energy of −218 kJ/mol ($\Delta E^{PBE+vdW}$).

For this binuclear site, it is clear that the N_2O dissociation is the rate controlling step. Thus, it can be argued that the hydroxylated

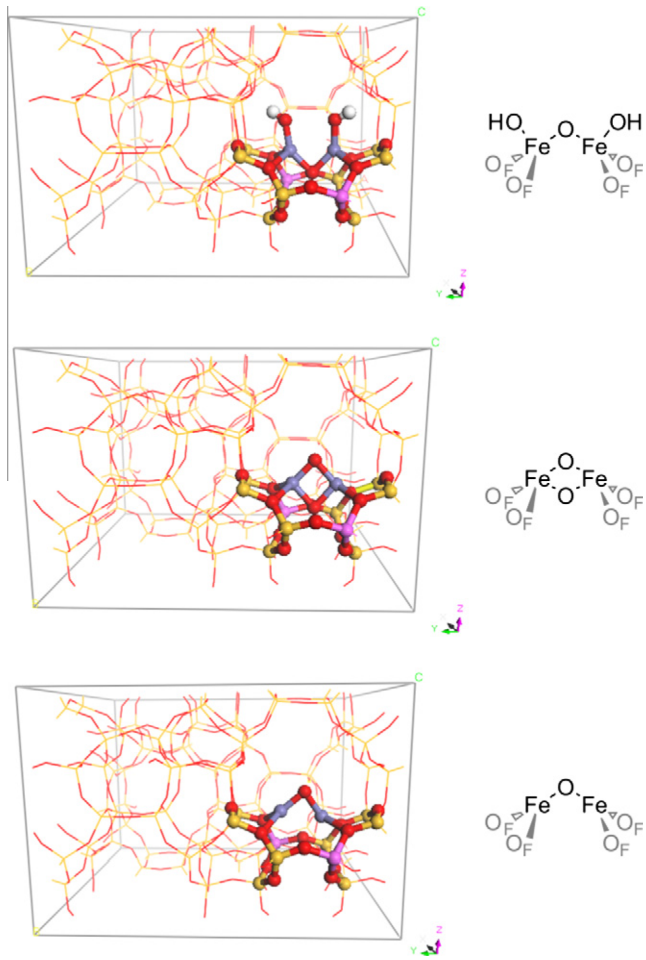

Fig. 8. Optimized structures of $[HOFe(\mu\text{-}O)FeOH]^{2+}$, $[Fe(\mu\text{-}O)_2Fe]^{2+}$ and $[Fe(\mu\text{-}O)Fe]^{2+}$ complexes in ZSM-5.

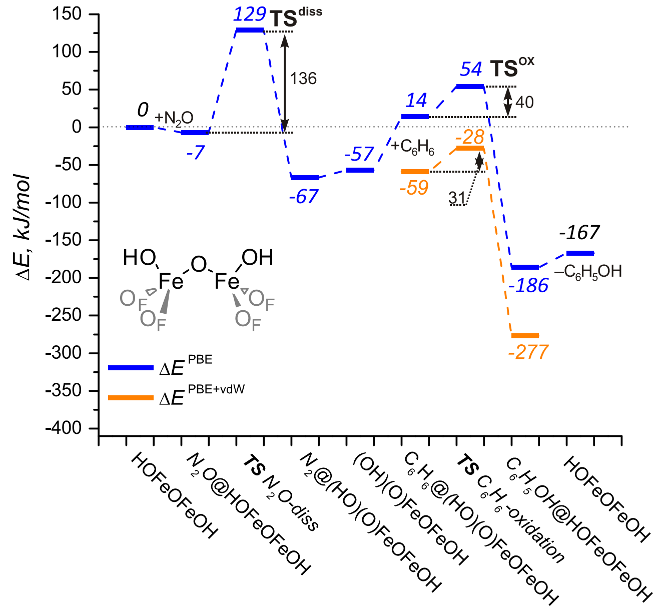

Fig. 9. Reaction energy diagram for benzene oxidation to phenol by N_2O over a binuclear $[HOFe(\mu\text{-}O)FeOH]^{2+}$ complex in ZSM-5.

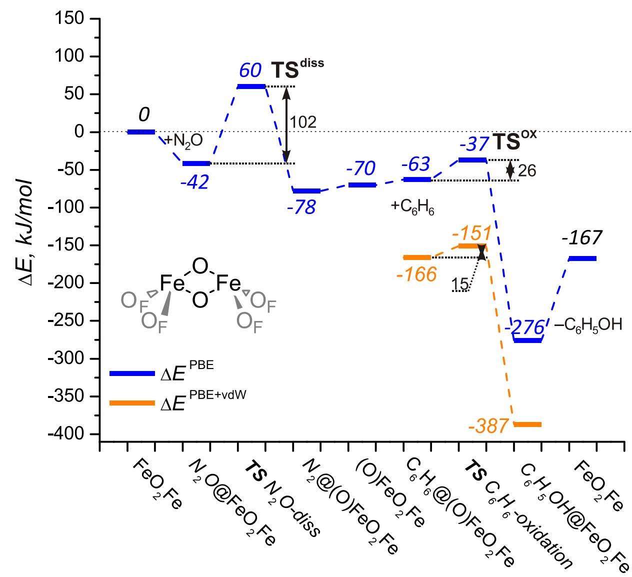

Fig. 10. Reaction energy diagram for benzene oxidation to phenol by N_2O over a binuclear $[Fe(\mu\text{-}O)_2Fe]^{2+}$ complex in ZSM-5.

$[HOFe(\mu\text{-}O)FeOH]^{2+}$ complex is not relevant for the oxidation activity of Fe/ZSM-5 catalysts, because it is generally accepted that N_2O dissociation to produce the oxidizing oxygen atom is easier than the subsequent reaction steps. The finding that for this complex N_2O activation is difficult is in line with the cluster modeling predictions by Heyden et al. [50]. In situ Raman and IR spectroscopic results also showed that the presence of H_2O on Fe/ZSM-5 leads to a decrease in the activity of N_2O decomposition, which is associated with the hydroxylation of the active dehydroxylated binuclear Fe sites to the hydroxylated structures [107].

3.2.3. *Reaction mechanism of benzene oxidation on $[Fe(\mu\text{-}O)_2Fe]^{2+}$*

The di-μ-oxo-bridged diamond-shaped $[Fe(\mu\text{-}O)_2Fe]^{2+}$ complex is formed upon dehydration of the $[HOFe(\mu\text{-}O)FeOH]^{2+}$ complex. Water removal does not affect the formal oxidation state of the involved iron centers. The optimized structure is also included in Fig. 8. The reaction energy diagram for the oxidation of benzene to phenol is given in Fig. 10.

The coordination environment of the iron centers in the $[Fe(\mu\text{-}O)_2Fe]^{2+}$ species is distorted resulting in their notable coordination unsaturation, and hence, enhanced Lewis acidity. Similar to the cases of Fe^{2+}/α-1 and Fe^{2+}/β-1 discussed above, the increased Lewis acidity is evident from the substantial energy of molecular adsorption of N_2O ($E_{ads}^{PBE} = -42$ kJ/mol). The adsorbed N_2O dissociates over the $[Fe(\mu\text{-}O)_2Fe]^{2+}$ site resulting in the $[O\text{-}Fe(\mu\text{-}O)_2Fe]^{2+}$ complex with an activation barrier of 102 kJ/mol and a reaction energy of −36 kJ/mol. The thus formed terminal oxygen ligand is highly reactive toward benzene oxidation. The activation energies for benzene oxidation are only 26 and 15 kJ/mol before and after vdW correction, respectively. The reaction energy exceeds −200 kJ/mol. Subsequent phenol desorption is very difficult. The vdW-corrected phenol desorption energy equals 220 kJ/mol. The very strong interaction between the $[Fe(\mu\text{-}O)_2Fe]^{2+}$ complex and the adsorbed phenol is due to the enhanced Lewis acidity of the coordinatively unsaturated iron centers.

3.2.4. *Reaction mechanism of benzene oxidation on $[Fe(\mu\text{-}O)Fe]^{2+}$*

The reaction energy diagram for catalytic benzene oxidation by the $[Fe(\mu\text{-}O)Fe]^{2+}$ complex (Fig. 8) is shown in Fig. 11. The framework oxygens of the 8MR zeolitic cation site and the bridging extraframework ligand form a distorted tetrahedral coordination site for both Fe^{2+} ions. N_2O adsorption on this site is very weak,

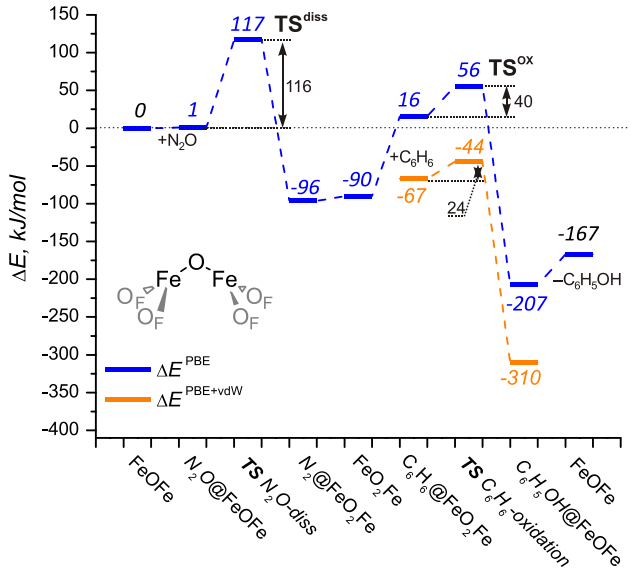

Fig. 11. Reaction energy diagram for benzene oxidation to phenol by N_2O over a binuclear $[Fe(\mu\text{-}O)Fe]^{2+}$ complex in ZSM-5.

and its dissociation proceeds with a high activation barrier (116 kJ/mol). The geometry of the resulting oxygenated complex $[Fe(\mu\text{-}O)_2Fe]^{2+}$ is substantially different from the structure discussed in Section 3.2.3. Instead of the diamond-shape structure, a boat conformation of the $[Fe(\mu\text{-}O)_2Fe]^{2+}$ is realized with highly reactive bridging oxygen ligands that readily oxidize benzene. This reaction step is exothermic and has low activation energy of 24 kJ/mol. The regeneration of the $[Fe(\mu\text{-}O)Fe]^{2+}$/ZSM-5 structure proceeds with a reaction energy ($\Delta E^{PBE+vdW}$ = 143 kJ/mol) close to that observed for the mononuclear sites.

3.2.5. Phenolate formation over binuclear iron sites

Similar to the case of the mononuclear $[FeO]^+$ sites, the close proximity of additional basic extraframework oxo- and hydroxy-ligands in the binuclear complexes opens a reaction path alternative to the closure of the catalytic cycle for benzene oxidation and results in the formation of grafted phenolate complexes. We investigated the required proton transfer reaction from adsorbed phenol to one of the extraframework oxygens bonded to the binuclear iron complex. The computed activation and reaction energies related to the adsorbed phenol state are summarized in Scheme 1. For all binuclear clusters, the formation of phenolates is exothermic. The calculated activation barriers are 29 and 65 kJ/mol for the $[Fe(\mu\text{-}O)Fe]^{2+}$ and $[Fe(\mu\text{-}O)_2Fe]^{2+}$ sites, respectively. The energy gain due to the formation of phenolate species for these sites is about 30 kJ/mol. In the case of the hydroxylated $[HOFe(\mu\text{-}O)FeOH]^{2+}$ binuclear cluster, the proton transfer from the adsorbed phenol to hydroxyl ligand proceeds with a low activation barrier of 24 kJ/mol and stabilizes the final complex by 71 kJ/mol. Thus, the regeneration of the binuclear iron sites upon the catalytic benzene oxidation via phenol desorption is blocked because of the formation of grafted phenolate species. This deactivation path is exothermic and proceeds with low activation barriers over all binuclear sites considered here.

4. Discussion

4.1. Stability of exchangeable Fe^{2+} ions in ZSM-5 zeolite

The main result of the comparison of the stability of ferrous ions at cation exchange sites of the ZSM-5 is their high stability at 6MR units. The most stable configuration is Fe^{2+} at the δ-1 site, involving a symmetric coordination environment of Fe^{2+} to four framework oxygen anions, each coordinating to one Al T atom. When the Al substitutions are placed at different framework positions of the δ site in such way that the symmetry of the negative framework charge is broken, the zeolite lattice becomes distorted. Obviously, these configurations are less preferred for Fe^{2+}. Similar but more pronounced distortions were found for Fe^{2+} at the α and β sites of ZSM-5. These distortions are driven by the tendency of the more basic oxygen ions of the anionic $[AlO_2]^-$ units to form direct interactions with the extraframework cation and may lead to destabilization of Fe^{2+} adsorption by values up to 120 kJ/mol. For the case when the cation charge is compensated by only one Al^{3+} in the direct coordination environment (with the other $[AlO_2]^-$ in an adjacent zeolite ring), the system is also substantially destabilized (+200 kJ/mol). The preference of the location of Fe^{2+} at the 6MR in the ZSM-5 lattice is in good agreement with the findings of Benco et al., who investigated the location of Fe^{2+} in ferrierite [94]. The stabilization within smaller 5MR units of the ZSM-5 lattice is less favorable, mainly due to inability to form a square-planar coordination environment of iron as is the case for the 6MR units. The high flexibility of the 8MR allows lattice oxygen to efficiently shield the exchangeable Fe^{2+} cations resulting in their relatively high stability at the γ-1 site.

4.2. Reactivity of extraframework iron-containing complexes in ZSM-5 zeolite

The catalytic cycle for benzene oxidation to phenol with nitrous oxide involves the dissociative adsorption of N_2O to form an extraframework oxygen species followed by the oxidation of benzene to phenol. The activation barriers for the oxygenation of the mononuclear Fe^{2+} species at various zeolitic sites lie between 59 (Fe^{2+}/δ-1) and 82 (Fe^{2+}/α-1) kJ/mol. These values are close to those computed for isolated Fe^{2+} ions in a periodic model ferrierite [57].

Alternative mononuclear Fe^{3+} and binuclear Fe^{2+} and Fe^{3+} complexes are generally less reactive for the initial dissociative adsorption of N_2O. Whereas in the case of $[FeO]^+$ at the δ-1 site, the calculated activation barrier for N_2O dissociation only slightly exceeds that for Fe^{2+}/δ-1 and lies in the range of 73–94 kJ/mol depending on the spin state, the barriers for the binuclear ferric complexes are much higher: 116, 102 and 136 kJ/mol for $[Fe(\mu\text{-}O)Fe]^{2+}$, $[Fe(\mu\text{-}O)_2Fe]^{2+}$ and $[HOFe(\mu\text{-}O)FeOH]^{2+}$, respectively. The activation barrier for $[HOFe(\mu\text{-}O)FeOH]^{2+}$ is the highest among the complexes considered in this study. This is in line with the trends found by Hansen et al. [50] and Xia et al. [107]. The iron ions in the binuclear complexes form a (distorted) tetrahedral coordination environment with the framework and extraframework oxygen ions. The introduction of an additional oxygen ligand into their first coordination sphere upon N_2O dissociation is associated with substantial structural perturbations. This decreases the reactivity of the binuclear iron complexes compared to the mononuclear species, in which an open coordination is readily available for the dissociating N_2O molecule.

Concerning the first step (dissociative adsorption of N_2O), we compared the reaction energies for the reaction $N_2O + Fe^{2+} \rightarrow [FeO]^{2+} + N_2$ to the stabilities of Fe^{2+} at the zeolite lattice. Benco et al. have argued that the stability of a cation and its reactivity – in that case toward NO – can be related to the Lewis acidity of the cation [94]. It is generally believed that less stable sites exhibit a higher reactivity [91,95]. In our case, no clear correlation was found between the reaction energy for N_2O dissociation and the relative stability of the Fe^{2+} site. Whereas the reaction energy for the most stable δ-1 configuration equals −57 kJ/mol, it is only 9 kJ/mol more exothermic for the D-4 site, which is less stable by

200 kJ/mol. This suggests that the local coordination environment has only a minor effect on the reactivity of Fe^{2+}.

The most important conclusion of this part is that the initial dissociative adsorption of N_2O to form a reactive extraframework oxygen atom proceeds with a relatively moderate barrier (60–90 kJ/mol) for isolated Fe^{2+} and FeO^+ with a preference for the isolated ferrous ions. The barriers are higher for binuclear iron complexes. In support of these findings are experimental data showing that N_2O dissociation occurs at relatively low temperature. This property has been used to titrate the density of Fe^{2+} sites in Fe/ZSM-5 sites [23]. One should note that the catalytic N_2O decomposition involves recombination of extraframework O atoms formed upon the dissociatiative adsorption of N_2O. This process is easier over the binuclear sites. In this case, the formation of O_2 is the rate limiting step, and it proceeds with higher barriers. The catalytic decomposition of N_2O therefore requires higher reaction temperatures compared to benzene oxidation [38].

Inspection of the reaction energy diagrams of the complete catalytic cycles for benzene oxidation over the most stable Fe^{2+} locations at δ-1, α-1 and β-1 sites (Figs. 4, 6 and 7) indicates that the activation barriers for N_2O dissociation and benzene oxidation are very close. The most pronounced difference in the catalytic behavior of Fe^{2+} at δ-1, α-1 and β-1 configurations is the stabilization of benzene and phenol at these sites that becomes apparent after considering the vdW corrections. The unfavorable confinement of benzene close to the Fe^{2+}/α-1 and Fe^{2+}/β-1 sites destabilizes the reaction intermediates and lowers the desorption energy of phenol and, accordingly, favors the closure of the catalytic cycle. Despite these differences between the 6MR exchange sites, it turns out that the overall barrier only slightly depends on the coordination of Fe^{2+} to the zeolite.

For all the alternative catalytic sites, the kinetic parameters for benzene hydroxylation and phenol desorption are found to be very comparable to the values for isolated Fe^{2+}. Binuclear iron complexes in their oxygenated states oxidize benzene with very low activation barriers of 15–30 kJ/mol (Figs. 9–11). However, the initial N_2O dissociation step is more difficult for these binuclear complexes suggesting that they are most likely not involved in benzene oxidation. Nevertheless, by analysis of the reaction energy diagrams in Figs. 4–8 and 9–11, it is not possible to completely exclude the contribution of mononuclear $[FeO]^+$ or binuclear Fe^{2+} and Fe^{3+} sites for oxidation of benzene to phenol. An important reason to exclude them as potential catalytic reaction centers turns out to be the presence of at least one additional extraframework basic oxygen anion that can act as a proton acceptor. This extra oxygen ligand opens an alternative reaction pathway that may lead to deactivation of the active site. Indeed, in all these cases, the OH group of adsorbed phenol can heterolytically dissociate over the $Fe^{\delta+}\cdots O^{\delta-}$ acid base pair yielding a phenolate species ($C_5H_6O^-$) and an OH group grafted to iron sites. This reaction is thermodynamically favored and proceeds with very low activation energies for all sites containing extraframework oxygen species (Scheme 1). The formation of such a stable phenolate intermediate is more favorable than the regeneration of the extraframework iron complexes. The formation of Fe(III)-phenolate complex was also evidenced in a combined UV–Vis and Raman study [29]. Dissociation of phenol over the isolated exchangeable Fe^{2+} sites is strongly unfavored thermodynamically. Accordingly, it is reasonable to suggest that despite the competing reactivity of $[FeO]^+$ and oxygen/hydroxy-bridged binuclear Fe^{2+}/Fe^{3+} complexes, these sites deactivate due to irreversible adsorption of a phenolate complex following benzene oxidation. The thus formed grafted hydrocarbon species can play a role of the intrazeolitic coke precursors and substantially decrease the accessability of the zeolitic voids. This deactivating reaction pathway is not possible for the isolated Fe^{2+} ions.

5. Conclusions

A comprehensive DFT study on the stability and reactivity of ferrous and ferric ions in a periodic ZSM-5 model has been carried out. The stability of Fe^{2+} strongly depends on the flexibility of the zeolitic site to which it coordinates and the distribution of the charge-compensating Al substitutions in the zeolite lattice. The preferred location of isolated Fe^{2+} involves six-membered rings with a symmetric distribution of framework Al atoms within the same ring. When these requirements are not met, iron will be present as isolated $[FeO]^+$ and oxygen/hydroxy-bridged binuclear Fe^{2+} and Fe^{3+} complexes.

The intrinsic reactivity of the Fe^{2+} in ZSM-5 zeolite in the catalytic oxidation of benzene to phenol with N_2O depends only slightly on the local coordination environment of the ferrous ion. The confinement effect exerted by the zeolite cage on the hydrocarbon reactant and product in the vicinity of Fe^{2+} affects the reaction energy diagram. Such steric constraints lead to more facile desorption of phenol and regeneration of the active Fe^{2+} site. Accordingly, the most preferred catalytic pathway is the oxidation of benzene to phenol catalyzed by Fe^{2+} at the α- and β-site.

Oxygen-containing mono- and binuclear Fe^{2+} and Fe^{3+} complexes are also potential sites for the formation of phenol, although the initial formation of the reactive oxygen atom via the dissociation adsorption of N_2O is considerably less favorable for the binuclear complexes. The overall reaction is however not catalytic because of the presence of highly basic oxygen ligands in the active Fe complexes. These basic oxygen anions favor dissociation of adsorbed phenol as compared to desorption, leading to the formation of stable phenolates that are difficult to desorb under practical conditions.

Acknowledgments

This work was financially supported by the Programme for Strategic Scientific Alliances between China and Netherlands (2008DFB50130) and the National Natural Science Foundation of China (20921092). NWO-NCF (SH-170-11) is acknowledged for providing access to the supercomputer facilities.

Appendix A. Supplementary material

Supplementary data associated with this article can be found, in the online version, at doi:10.1016/j.jcat.2011.07.008.

References

[1] G.I. Panov, V.I. Sobolev, A.S. Kharitonov, J. Mol. Catal. 61 (1990) 85.
[2] G.I. Panov, G.A. Sheveleva, A.S. Kharitonov, V.N. Romannikov, L.A. Vostrikova, Appl. Catal. A: Gen. 82 (1992) 31.
[3] F. Kapteijn, G. Marban, J. RodriguezMirasol, J.A. Moulijn, J. Catal. 167 (1997) 256.
[4] G.I. Panov, A.K. Uriarte, M.A. Rodkin, V.I. Sobolev, Catal. Today 41 (1998) 365.
[5] G. Centi, S. Perathoner, F. Vazzana, M. Marella, M. Tomaselli, M. Mantegazza, Adv. Environ. Res. 4 (2000) 325.
[6] E.M. El-Malki, R.A. van Santen, W.M.H. Sachtler, Micropor. Mesopor. Mater. 35–36 (2000) 235.
[7] J. Perez-Ramirez, F. Kapteijn, G. Mul, J.A. Moulijn, Chem. Commun. (2001) 693.
[8] Q. Zhu, E.J.M. Hensen, B.L. Mojet, J. van Wolput, R.A. van Santen, Chem. Commun. (2002) 1232.
[9] K. Sun, H. Xia, E. Hensen, R. van Santen, C. Li, J. Catal. 238 (2006) 186.
[10] K.A. Dubkov, V.I. Sobolev, G.I. Panov, Kinet. Catal. 39 (1998) 72.
[11] K.A. Dubkov, V.I. Sobolev, E.P. Talsi, M.A. Rodkin, N.H. Watkins, A.A. Shteinman, G.I. Panov, J. Mol. Catal. A: Chem. 123 (1997) 155.
[12] E.J.M. Hensen, Q. Zhu, R.A. van Santen, J. Catal. 220 (2003) 260.
[13] L.V. Pirutko, V.S. Chernyavsky, A.K. Uriarte, G.I. Panov, Appl. Catal. A: Gen. 227 (2002) 143.
[14] P. Kubanek, B. Wichterlova, Z. Sobalik, J. Catal. 211 (2002) 109.
[15] E.J.M. Hensen, Q.J. Zhu, P.-H. Liu, K.-J. Chao, R.A. van Santen, J. Catal. 226 (2004) 466.
[16] G.I. Panov, A.S. Kharitonov, V.I. Sobolev, Appl. Catal. A: Gen. 98 (1993) 1.

[17] S.H. Choi, B.R. Wood, J.A. Ryder, A.T. Bell, J. Phys. Chem. B 107 (2003) 11843.
[18] J.F. Jia, K.S. Pillai, W.M.H. Sachtler, J. Catal. 221 (2004) 119.
[19] E.J.M. Hensen, Q. Zhu, R.A.J. Janssen, P. Magusin, P.J. Kooyman, R.A. van Santen, J. Catal. 233 (2005) 123.
[20] E.J.M. Hensen, Q. Zhu, R.A. van Santen, J. Catal. 233 (2005) 136.
[21] K. Yoshizawa, Y. Shiota, T. Yamabe, J. Am. Chem. Soc. 121 (1998) 147.
[22] G. Marban, T. Valdes-Solis, A.B. Fuertes, J. Catal. 226 (2004) 138.
[23] K.A. Dubkov, N.S. Ovanesyan, A.A. Shteinman, E.V. Starokon, G.I. Panov, J. Catal. 207 (2002) 341.
[24] V.S. Chemyavsky, L.V. Pirutko, A.K. Uriarte, A.S. Kharitonov, G.I. Panov, J. Catal. 245 (2007) 466.
[25] R. Joyner, M. Stockenhuber, J. Phys. Chem. B 103 (1999) 5963.
[26] S.H. Choi, B.R. Wood, A.T. Bell, M.T. Janicke, K.C. Ott, J. Phys. Chem. B 108 (2004) 8970.
[27] L.J. Lobree, I.C. Hwang, J.A. Reimer, A.T. Bell, J. Catal. 186 (1999) 242.
[28] J. Perez-Ramirez, M.S. Kumar, A. Bruckner, J. Catal. 223 (2004) 13.
[29] H. Xia, K. Sun, K. Sun, Z. Feng, W.X. Li, C. Li, J. Phys. Chem. C 112 (2008) 9001.
[30] A.A. Battiston, J.H. Bitter, D.C. Koningsberger, Catal. Lett. 66 (2000) 75.
[31] A.A. Battiston, J.H. Bitter, F.M.F. de Groot, A.R. Overweg, O. Stephan, J.A. van Bokhoven, P.J. Kooyman, C. van der Spek, G. Vank, D.C. Koningsberger, J. Catal. 213 (2003) 251.
[32] A.A. Battiston, J.H. Bitter, W.M. Heijboer, F.M.F. de Groot, D.C. Koningsberger, J. Catal. 215 (2003) 279.
[33] A.A. Battiston, J.H. Bitter, D.C. Koningsberger, J. Catal. 218 (2003) 163.
[34] P. Marturano, L. Drozdov, A. Kogelbauer, R. Prins, J. Catal. 192 (2000) 236.
[35] P. Marturano, L. Drozdova, G.D. Pirngruber, A. Kogelbauer, R. Prins, Phys. Chem. Chem. Phys. 3 (2001) 5585.
[36] J.F. Jia, Q. Sun, B. Wen, L.X. Chen, W.M.H. Sachtler, Catal. Lett. 82 (2002) 7.
[37] H. Xia, K. Sun, Z. Liu, Z. Feng, P. Ying, C. Li, J. Catal. 270 (2010) 103.
[38] K. Sun, H. Xia, Z. Feng, R. van Santen, E. Hensen, C. Li, J. Catal. 254 (2008) 383.
[39] H. Xia, K. Sun, F. Fan, K. Sun, W. Su, Z. Feng, P. Ying, C. Li, J. Catal. 259 (2008) 269.
[40] H. Xia, S.D. Fleischman, C. Li, S.L. Scott, J. Phys. Chem. Lett. 2 (2011) 190.
[41] Y. Li, H. Xia, F. Fan, Z. Feng, R.A. van Santen, E.J.M. Hensen, C. Li, Chem. Commun. (2008) 774.
[42] G.D. Pirngruber, P.K. Roy, R. Prins, Phys. Chem. Chem. Phys. 8 (2006) 3939.
[43] A. Zecchina, M. Rivallan, G. Berlier, C. Lamberti, G. Ricchiardi, Phys. Chem. Chem. Phys. 9 (2007) 3483.
[44] J. Perez-Ramirez, G. Mul, F. Kapteijn, J.A. Moulijn, A.R. Overweg, A. Domenech, A. Ribera, I. Arends, J. Catal. 207 (2002) 113.
[45] J.A. Ryder, A.K. Chakraborty, A.T. Bell, J. Phys. Chem. B 106 (2002) 7059.
[46] J.A. Ryder, A.K. Chakraborty, A.T. Bell, J. Catal. 220 (2003) 84.
[47] A. Heyden, B. Peters, A.T. Bell, F.J. Keil, J. Phys. Chem. B 109 (2005) 1857.
[48] A. Heyden, A.T. Bell, F.J. Keil, J. Catal. 233 (2005) 26.
[49] A.L. Yakovlev, G.M. Zhidomirov, R.A. van Santen, J. Phys. Chem. B 105 (2001) 12297.
[50] N. Hansen, A. Heyden, A.T. Bell, F.J. Keil, J. Phys. Chem. C 111 (2007) 2092.
[51] N. Hansen, A. Heyden, A.T. Bell, F.J. Keil, J. Catal. 248 (2007) 213.
[52] L. Kiwi-Minsker, D.A. Bulushev, A. Renken, J. Catal. 219 (2003) 273.
[53] L. Kiwi-Minsker, D.A. Bulushev, A. Renken, Catal. Today 91–92 (2004) 165.
[54] L. Kiwi-Minsker, D.A. Bulushev, A. Renken, Catal. Today 110 (2005) 191.
[55] H. Guesmi, D. Berthomieu, L. Kiwi-Minsker, J. Phys. Chem. C 112 (2008) 20319.
[56] H. Guesmi, D. Berthomieu, B. Bromley, B. Coq, L. Kiwi-Minsker, Phys. Chem. Chem. Phys. 12 (2010) 2873.
[57] S. Sklenak, P.C. Andrikopoulos, B. Boekfa, B. Jansang, J. Novakova, L. Benco, T. Bucko, J. Hafner, J. Dedecek, Z. Sobalik, J. Catal. 272 (2010) 262.
[58] K. Yoshizawa, Y. Shiota, T. Yumura, T. Yamabe, J. Phys. Chem. B 104 (2000) 734.
[59] N.A. Kachurovskaya, G.M. Zhidomirov, R.A. van Santen, J. Phys. Chem. B 108 (2004) 5944.
[60] M.F. Fellah, I. Onal, Turkish J. Chem. 33 (2009) 333.
[61] M.F. Fellah, R.A. van Santen, I. Onal, J. Phys. Chem. C 113 (2009) 15307.
[62] M.F. Fellah, I. Onal, R.A. van Santen, J. Phys. Chem. C 114 (2010) 12580.
[63] E.A. Pidko, E.J.M. Hensen, G.M. Zhidomirov, R.A. van Santen, J. Catal. 255 (2008) 139.
[64] E.A. Pidko, R.A. van Santen, E.J.M. Hensen, Phys. Chem. Chem. Phys. 11 (2009) 2893.
[65] L. Benco, T. Bucko, J. Hafner, J. Phys. Chem. C 113 (2009) 18807.
[66] N. Hansen, T. Kerber, J. Sauer, A.T. Bell, F.J. Keil, J. Am. Chem. Soc. 132 (2010) 11525.
[67] S. Svelle, C. Tuma, X. Rozanska, T. Kerber, J. Sauer, J. Am. Chem. Soc. 131 (2009) 816.
[68] I.L.C. Buurmans, E.A. Pidko, J.M. de Groot, E. Stavitski, R.A. van Santen, B.M. Weckhuysen, Phys. Chem. Chem. Phys. 12 (2010) 7032.
[69] E. Stavitski, E.A. Pidko, M.H.F. Kox, E.J.M. Hensen, R.A. van Santen, B.M. Weckhuysen, Chem. Eur. J. 16 (2010) 9340.
[70] G. Kresse, J. Hafner, Phys. Rev. B 48 (1993) 13115.
[71] G. Kresse, J. Hafner, Phys. Rev. B 49 (1994) 14251.
[72] G. Kresse, J. Furthmuller, Comput. Mater. Sci. 6 (1996) 15.
[73] G. Kresse, J. Furthmuller, Phys. Rev. B 54 (1996) 11169.
[74] P.E. Blochl, Phys. Rev. B 50 (1994) 17953.
[75] G. Kresse, D. Joubert, Phys. Rev. B 59 (1999) 1758.
[76] J.P. Perdew, K. Burke, M. Ernzerhof, Phys. Rev. Lett. 77 (1996) 3865.
[77] H.J. Monkhorst, J.D. Pack, Phys. Rev. B 13 (1976) 5188.
[78] H. van, Acta Crystallogr. Sect. B 46 (1990) 731.
[79] C. Baerlocher, L.B. McCusker, Database of Zeolite Structures. <http://www.iza-structure.org/databases/>.
[80] G. Mills, H. Jonsson, G.K. Schenter, Surf. Sci. 324 (1995) 305.
[81] D.H. Kitson, A.T. Hagler, Biochemistry 27 (1988) 7176.
[82] P. Dauberosguthorpe, V.A. Roberts, D.J. Osguthorpe, J. Wolff, M. Genest, A.T. Hagler, Proteins Struct. Funct. Genet. 4 (1988) 31.
[83] T. Demuth, L. Benco, J. Hafner, H. Toulhoat, F. Hutschka, J. Chem. Phys. 114 (2001) 3703.
[84] A.M. Vos, X. Rozanska, R.A. Schoonheydt, R.A. van Santen, F. Hutschka, J. Hafner, J. Am. Chem. Soc. 123 (2001) 2799.
[85] J.D.Z. Gale, Kristall 220 (2005) 552.
[86] T.J. Hou, L.L. Zhu, X.J. Xu, J. Phys. Chem. B 104 (2000) 9356.
[87] H. Jobic, H. Ramanan, S.M. Auerbach, M. Tsapatsis, P. Fouquet, Micropor. Mesopor. Mater. 90 (2006) 307.
[88] E.A. Pidko, R.A. van Santen, Zeolites and Catalysis: Synthesis, Reactions and Applications, Wiley-VCH Verlag GmbH & Co. KGaA, 2010.
[89] J. Dedecek, D. Kaucky, B. Wichterlova, Micropor. Mesopor. Mater. 35–36 (2000) 483.
[90] E.A. Pidko, R.A. van Santen, J. Phys. Chem. C 111 (2007) 2643.
[91] E.A. Pidko, V.B. Kazansky, E.J.M. Hensen, R.A. van Santen, J. Catal. 240 (2006) 73.
[92] E.A. Pidko, E.J.M. Hensen, R.A. van Santen, J. Phys. Chem. C 111 (2007) 13068.
[93] J. Dedecek, B. Wichterlova, Phys. Chem. Chem. Phys. 1 (1999) 629.
[94] L. Benco, T. Bucko, R. Grybos, J. Hafner, Z. Sobalik, J. Dedecek, J. Hrusak, J. Phys. Chem. C 111 (2007) 586.
[95] L. Benco, T. Bucko, J. Hafner, H. Toulhoat, J. Phys. Chem. B 109 (2005) 20361.
[96] D. Nachtigallova, P. Nachtigall, M. Sierka, J. Sauer, J. Phys. Chem. Chem. Phys. 1 (1999) 2019.
[97] Q. Zhu, B.L. Mojet, R.A. Janssen, E.J.M. Hensen, J. van Grondelle, P. Magusin, R.A. van Santen, Catal. Lett. 81 (2002) 205.
[98] Y. Shiota, K. Suzuki, K. Yoshizawa, Organometallics 25 (2006) 3118.
[99] W.Z. Liang, A.T. Bell, M. Head-Gordon, A.K. Chakraborty, J. Phys. Chem. B 108 (2004) 4362.
[100] C.R.F. Lund, J. Catal. 243 (2006) 438.
[101] B.R. Wood, J.A. Reimer, A.T. Bell, M.T. Janicke, K.C. Ott, J. Catal. 224 (2004) 148.
[102] E.M. El-Malki, R.A. van Santen, W.M.H. Sachtler, J. Phys. Chem. B 103 (1999) 4611.
[103] H.-Y. Chen, W.M.H. Sachtler, Catal. Today 42 (1998) 73.
[104] A. Heyden, N. Hansen, A.T. Bell, F.J. Keil, J. Phys. Chem. B 110 (2006) 17096.
[105] M.J. Rice, A.K. Chakraborty, A.T. Bell, J. Phys. Chem. B 104 (2000) 9987.
[106] E.J.M. Hensen, E.A. Pidko, N. Rane, R.A. van Santen, Angew. Chem. Int. Ed. 46 (2007) 7273.
[107] H. Xia, K. Sun, Z. Feng, C. Li, J. Phys. Chem. C 115 (2011) 542.